**COLLECTIVE CELL GUIDANCE BY COOPERATIVE INTERCELLULAR FORCES.**
**Supporting Online Material**

DT Tambe, CC Hardin, TE Angelini, K Rajendran, CY Park, X Serra-Picamal, EH Zhou, MH Zaman, JP Butler, DA Weitz, JJ Fredberg, X Trepat

***Supplement 1. Monolayer Stress Microscopy.***

Within the monolayer, physical forces are transmitted between each cell and its substrate, which are called traction forces, and between each cell and its immediate neighbors, which are called the intercellular forces (Fig. S1). The local intercellular force per unit area of contact defines the local intercellular stress, which comprises two mutually independent components: the normal stress (depicted as red arrows acting perpendicular to the local cell-cell junction) and the shear stress (depicted as a blue arrow acting parallel to the local cell-cell junction). These stresses at the cell-cell junction necessarily extend into and become supported by mechanical stresses within the cell body.

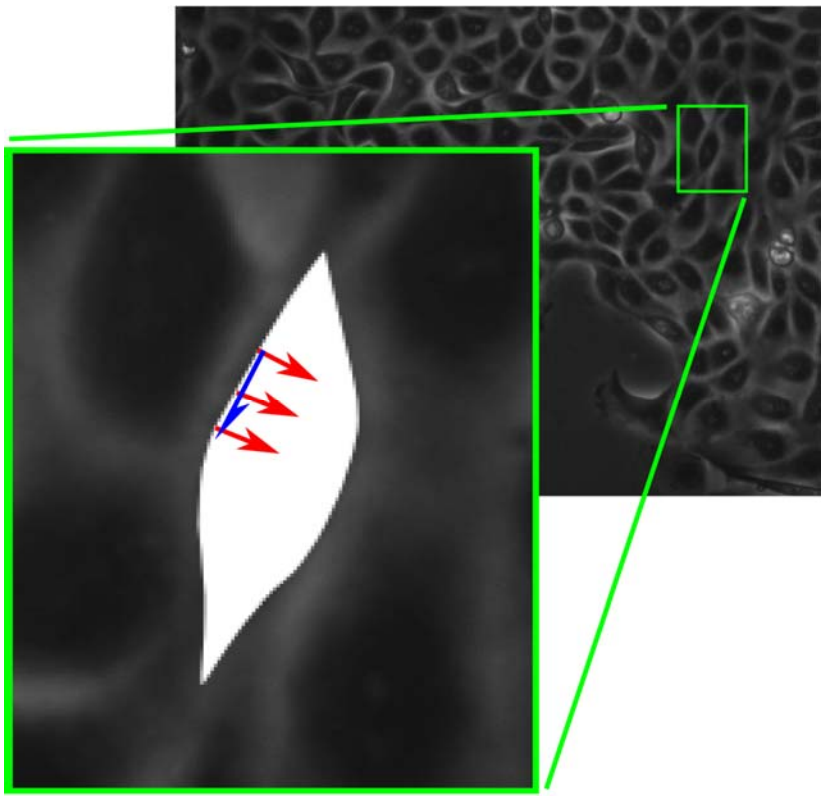

**Figure S1 | Mechanical forces in sheet of migrating cells**.

We have previously introduced a method to measure the distribution of traction forces that an advancing cellular monolayer exerts on its substrate.[1, 2] Here we build upon that approach in order to measure not just those traction forces, but from these data to measure the intercellular normal stresses and shear stresses that each cell exerts upon its immediate neighbors.

***General approach:*** The intercellular stress is a local outcome of the overall balance of cell-substrate tractions across the entire monolayer as demanded by Newton's laws. Traction forces exerted locally by each cell on the substrate are balanced at distances significantly larger than the size of the cell, however.[2] Local variations in monolayer height can induce moments and out-of-plane stresses in principle, but the lateral extent of the monolayers in question here is at least three orders of magnitude greater than the thickness, and that thickness is approximately uniform (Fig. S4). Such a system therefore lends itself naturally to a formal two-dimensional balance of line tensions (force per unit length) in a system of zero thickness, and makes recovery of intercellular line tensions rigorous.

Only as a matter of computational convenience, we calculate this two-dimensional force balance within the monolayer by representing the cellular monolayer instead as a thin elastic sheet. This is permissible because, if the traction distribution is known, then the force balance itself does not depend upon cell material properties. Line tensions (in units of force per unit length) and the more familiar units of stress (force per unit area) are related through a uniform monolayer height, h (Supplement 4), but the underlying force balance itself, being two-dimensional, does not depend upon the assumption of uniform cell height. For simplicity, therefore, and without loss of generality, the remainder of the text deals solely in terms of familiar stress components.

As such, the internal stress tensor $\sigma_{ij}(x,y)$ is treated as plane stress in the $x,y$ plane, where $i$ and $j$ run over the coordinates $x,y$; all stress components associated with the $z$ direction vanish. The measured local tractions $T_i(x,y)$ are the components of the shear stresses exerted *by* the cells *on* the substrate, and hence by Newton's third law, the forces exerted *by* the substrate *on* the monolayer are simply the negative of these tractions. Since at any instant there is no net force on the monolayer as a whole, these tractions must precisely balance the internal stresses generated within the monolayer. This balance of forces is formally represented by the equations of mechanical equilibrium,

$$\sigma_{ij,j} = T_i \qquad \text{(Eq. S1)}$$

where we use the Einstein convention of summation over repeated indices and $()_{,j}$ denotes $\partial / \partial x_j$. From the form of Eq. S1, it is clear that the source term on the right hand side can be thought of equivalently as a body force, although one that is nonuniform and time-varying. The internal stresses, $\sigma_{ij}$, are those required to balance the measured traction forces irrespective of whether monolayer material is active or passive, elastic or visco-elastic, linear or nonlinear. The key assumption is only that the monolayer is treated as a continuum.

***Boundary conditions and boundary artifacts:*** Eq. S1 describes an elliptical boundary value problem. Boundary conditions on the free edge of the monolayer were taken to be homogeneous in stress, $\sigma_{ij} n_j = 0$. Boundary conditions at the edges of the field of view (shown by red lines in **Fig. S2 a**) were taken as zero normal displacement, $u_j n_j = 0$, where $n_j$ denotes the components of the vector normal to the boundary. Imposition of this zero normal displacement condition is physically equivalent to continuing the monolayer outside the field of view as a mirror image, but this continuation introduces artifactual reaction forces along the boundary. Depending upon their spatial distribution, the stresses due to these reaction forces decay as $1/r$ or faster, but far from the edges the local stress field is dominated by the source term – the traction forces, $T_i$. As such, regions in which the boundary effects contribute appreciably to the result can be cropped out. Here we report measurements in a region that is beyond 130 μm from the field of view edges, as this inner region is largely free of boundary artifacts. To quantify associated errors we made scatter plots of average normal stresses within the inner as calculated from the maximum (actual) field of view edges against those calculated from successively smaller (cropped) fields of view. Up to a cropping distance of 60 μm from the maximum field of view, the average normal stresses within the inner region were strongly correlated ($r^2 > 0.98$, 0 < intercept< -20Pa, and 1 < slope < 0.95), thus establishing insensitivity of stresses in the inner region to the placement of the boundary.

***Principal stresses and principal orientations:*** Eigenvalue decomposition of the stress tensor defines the principal stresses ($\sigma_{\max}$ and $\sigma_{\min}$) and the corresponding mutually perpendicular eigenvectors define the local orientation of these stresses. By definition, each of these eigenvectors also defines the orientation of zero shear stress. We also compute the scalar tension within the sheet which is local average normal stress, defined as $(\sigma_{\max} + \sigma_{\min})/2$.

***Implementation by finite element analysis (FEA):*** Solving the equilibrium equations is equivalent to solving the boundary value problem of minimization of total potential energy per unit thickness of the monolayer defined by $\Pi = \iint_R \left( \frac{1}{2} \sigma_{ij} \varepsilon_{ij} - u_j T_j \right) dxdy$, where $\varepsilon_{ij}$ is the planar strain tensor, and $R$ is the bounded domain, subjected to the boundary conditions described above. We minimize this functional with respect to displacements $u_j(x,y)$ such that conditions at the domain boundaries are satisfied, as described

below. From these displacements, which are automatically compatible, we compute both strains and stresses in the monolayer.

As noted above, the specific material properties of the monolayer have no effect on the recovered distribution of intercellular forces. Without loss of generality, therefore, the monolayer is treated as an isotropic homogeneous elastic sheet with Young's modulus of 10kPa, Poisson's ratio of 0.5, and height of 5 μm. This sheet is uniformly discretized into four-node square elements (Fig S2, b, c) such that the FEA grid matches the traction grid recovered from FTTM. This grid is dense enough so that the internal stresses essentially independent of the size of elements.

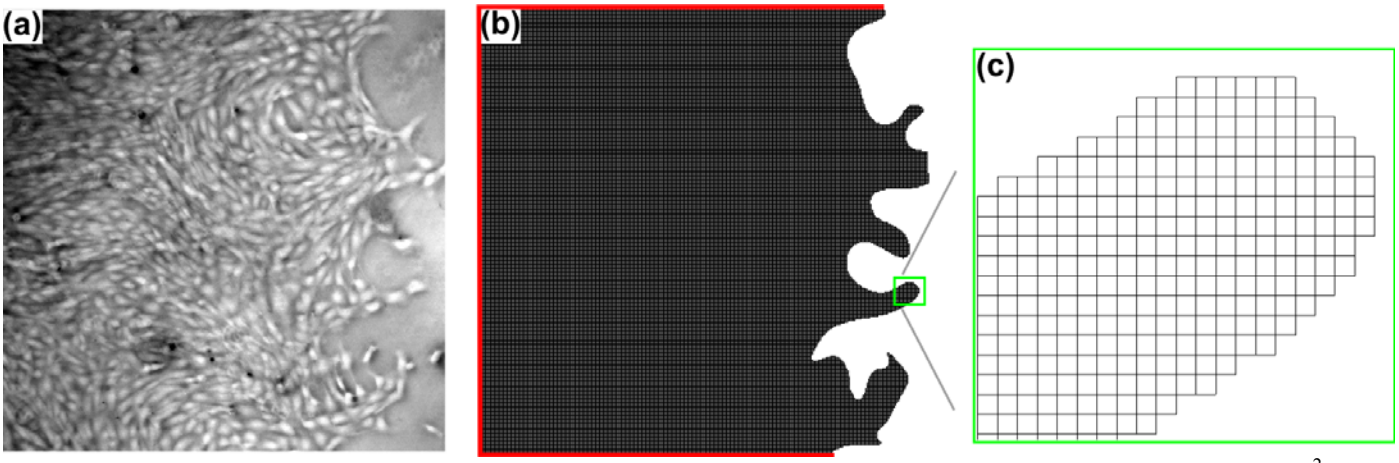


**Figure S2 | Finite element representation of monolayer.** (**a**) Image of a RPME cell monolayer (890×890 μm$^2$) bounded by a free edge on one side and edges defined by the field of view (red lines) on other three sides. (**b**) The monolayer is discretized uniformly with four node square elements. (**c**) Magnified view of a local region in (**b**) (each square is 2.61×2.61 μm$^2$).

This FEA scheme then transforms the boundary value problem into a system of linear equations, which are solved for the local displacements using standard Cholesky factorization. From these displacements we calculate stresses through the constitutive equation $\sigma_{ij} = \frac{2}{3} E\left(\varepsilon_{ij} + \varepsilon_{kk}\delta_{ij}\right)$ where $\delta_{ij}$ is the Kronecker delta. Explicitly, $\sigma_{xx}$ and $\sigma_{yy}$ are normal stresses along the laboratory $x-$ and $y-$axes, and $\sigma_{xy}(=\sigma_{yx})$ is the shear stress, also in the laboratory frame. Diagonalizing $\sigma_{ij}$ amounts to a rotation, equivalent to the eigenvalue decomposition noted above, from which the principal stresses are obtained, and in this rotated system the shear stresses are zero. The entire FEA scheme is implemented using an in-house FORTRAN90 program.

***Effect of isotropy and homogeneity of the material properties:*** Anisotropy and heterogeneity of material properties can influence the magnitude of stresses, but contribute only weakly to the recovery of orientation of planes with zero shear stress. This weak dependence is confirmed through the observation on RPME cells that the maximal principal stress orientations which are local axis of highest tension aligns with the cell orientation (Fig. 2 e and Fig S4) which, for these spindle-like cells, is largely orientation of actin stress fibers.

***Measurement of gel deformation:*** As described previously[2], traction forces were determined from gel deformations. Gel deformations were quantified from images of embedded fluorescent markers after correcting for microscope stage drift. By contrast with our previous report [2], however, here we corrected for stage drift using an improved and simplified method. We begin with a phase contrast image of cells and a fluorescent image of markers embedded near the surface of the gel, and then acquire subsequent image pairs at 5 minute intervals for a period of 3-4 hours. To correct for stage drift, in these subsequent fluorescent

images we matched embedded markers in an unstrained region of the gel with the same markers from the first fluorescent image. This drift correction was achieved with the help of an in-house image acquisition program developed using MATLAB. This technique of recording gel deformation provides highly reproducible and precise measurements. At the end of the experiment, cells were detached from the gel surface with isotonic 10X trypsin for 1 h followed by acquisition of drift corrected reference image of the fluorescent markers. All experiments were conducted in culture environment (37$^{o}$C, and 5% $CO_2$) on an inverted optical microscope at magnification 7.5X for RPME cells and 10X for other cells.

***Measurement of cellular velocities:*** The cellular velocity field within the monolayer is measured by particle imaging velocimetry (PIV). Specifically, an image from sequence of phase contrast images recorded at an interval $\Delta t$ is compared with the succeeding image. And window pairs, one to each image, are examined for cross correlation as a function of shifting window position. The shift of one window relative to the reference (window from image at earlier time) that maximizes the cross correlation function is taken as the displacement of the center of that window. Together with $\Delta t$, this determines the velocity of the central point of the reference window. This procedure is then repeated across the entire field, and a velocity map is constructed at each grid point in the pixelated plane. There is sufficient phase contrast between the cell interiors and the cell-cell boundary junctions such that this is a robust procedure within the sheet.

***Fourier-transform traction microscopy:*** Algorithm used for traction mapping is same as reported by Trepat et al [2].

***Supplement 2. Cell Culture.***

***Cell culture:*** All the cells were cultured on plastic flasks and incubated at 37ºC with 5% $CO_2$.

| **Cells** | **Medium** |
|---|---|
| Madin-Darby canine kidney cells (MDCK) (strain II) | Modified Eagle's medium (MEM) with Earle's salts supplemented with 5% fetal bovine serum (FBS), 2mM l-glutamine, 100U/ml penicillin, and 100 g/ml streptomycin |
| Rat pulmonary microvascular endothelial cells (RPMEC) | Roswell Park Memorial Institute (RPMI-1640) supplemented with 10% FBS, 100 U/ml penicillin and, 100 g/ml streptomycin, and Fungizone [3]. |
| MCF10A with overexpressing ErbB2<br>MCF10A with overexpressing HA-tagged 14-3-3ζ<br>MCF10A control (vector) | Dulbecco's modified Eagle's medium (DMEM)/F12 supplemented with 5% donor horse serum, 20 ng/ml epidermal growth factor (EGF), 10 lg/ml insulin, 0.5 lg/ml hydrocortisone, 100 ng/ml cholera toxin, and antibiotics [4] |

***Cell seeding:*** A 4μl drop of dense cell solution (8 million cells/ml) was gently suspended on the center of the gel containing 2ml media. The cells were then kept at 37$^{o}$C and 5% $CO_2$ for 48 hours to form confluent circular monolayer that migrates radially outwards.

***Preparation of polyacrylamide gel substrates:*** Polyacrylamide substrate preparation was similar to published protocol [2].

***Supplement 3. Tractions exerted by the cells on its substrate.***

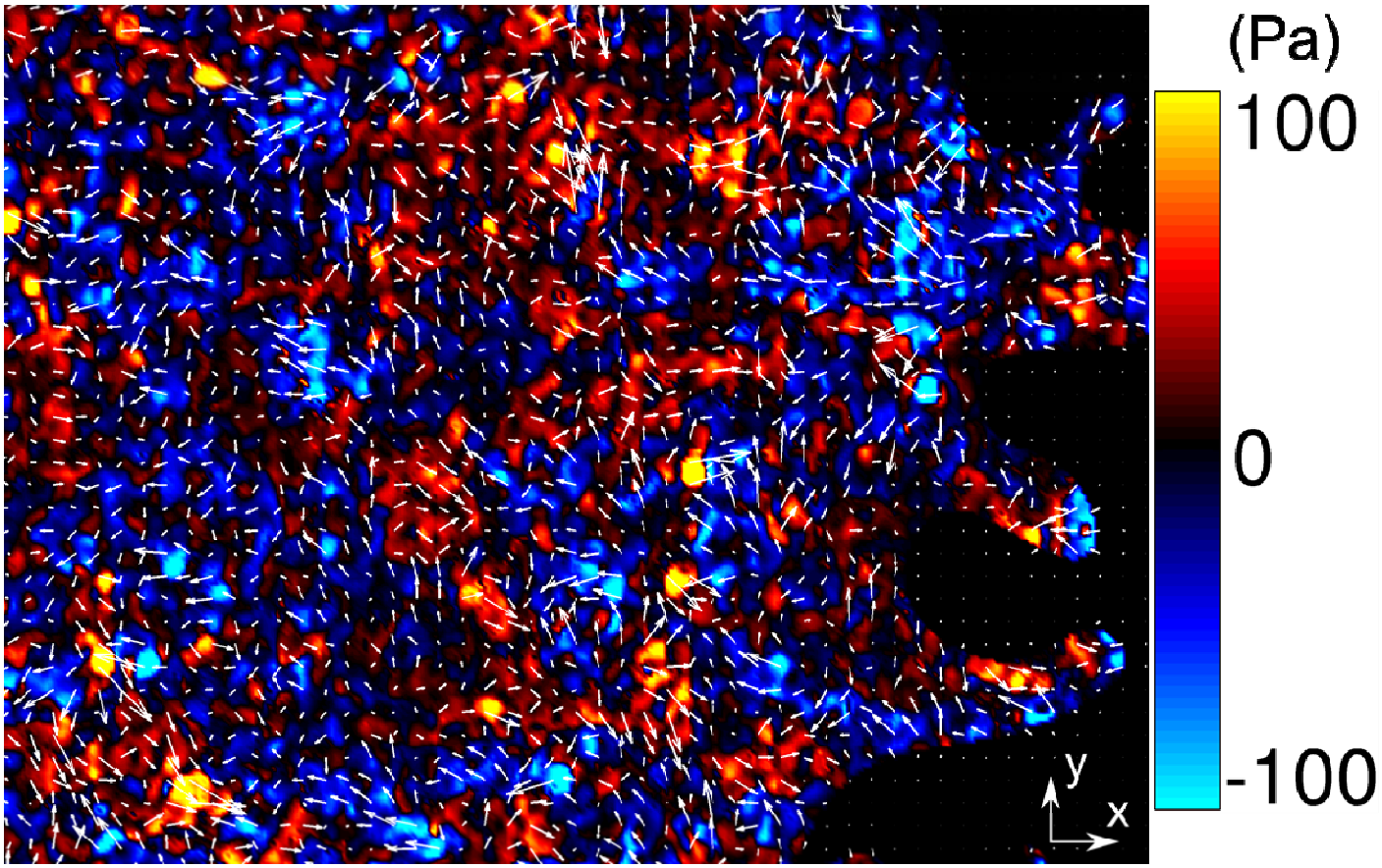


**Figure S3 | Traction forces exerted by the RPME monolayer upon its substrate.** Color-coded map of x-component of the traction force (corresponding to the monolayer shown in Fig. 2 a). Overlain upon this map are white arrows depicting complete traction vectors (both x and y components). Fluctuations of these tractions forces vary over length scales small compared with fluctuations of intercellular stresses (compare Fig. 2 b) because traction forces correspond to the gradient of those intercellular stresses (Eq. S1). Equivalently, Eq. S1 requires the rugged landscape of intercellular stress (Fig. 2b) to arise from the pile-up (accumulation) of these tractions forces.

***Supplement 4. Monolayer height and its variations.***

MSM is based upon nothing more than a rigorous two-dimensional force balance enforced in the cell plane. Since monolayer breadth greatly exceeds its height, a resulting state of plane stress provides computational convenience to the stress recovery procedure. Using confocal imaging of the monolayer we observe that, the first two cell rows excepted, monolayer height is roughly constant (Fig. S4). The recovered stress maps engenders errors in proportional to the ratio between the real and the assumed local monolayer height. As such, for regions greater than 20μm from the leading edge these errors would be smaller than 20%. Therefore, the profound ruggedness of the stress landscape and the associated long-range correlations of the maximum principal orientations cannot be attributed to these small variations in monolayer height.

**Figure S4 | Height of an MDCK monolayer expressing GFP-actin.** Cell height measured using confocal microscopy (60X). The coefficient of variation is close to 20%. The solid line is the mean height and the dotted lines are mean ± standard deviation.

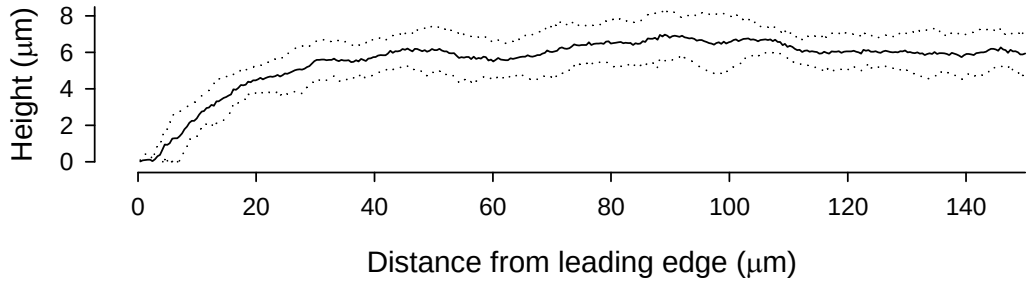


***Supplement 5. In the endothelial monolayer, the long axis of the cell tends to align with the orientation of local maximum principal stress.***

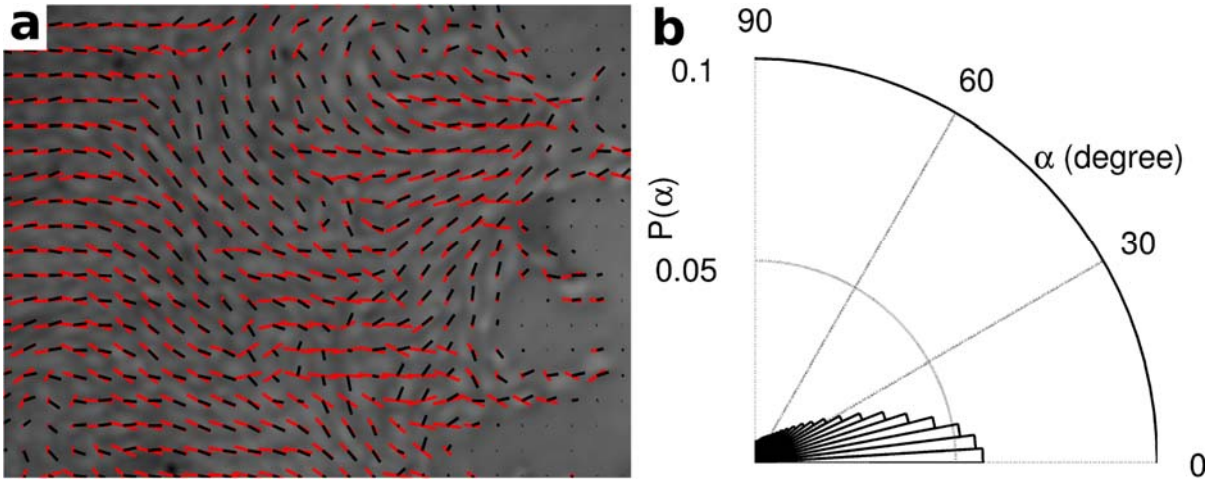


**Figure S5 | Cells in RPME monolayers align with the local orientation of maximum principal stress.** (**a**) Image of the RPME cell monolayer from Fig. 2 a. Shown here is an overlapped image of the orientation of long axis of the cells (black lines) and the orientation of maximum principal stresses (red lines). The local cellular orientation is the orientation of major axis of an ellipse that has same second-moments of 20x20 $\mu m^2$ region of the transmitted light image of the monolayer. The map of cell orientation is generated using image processing toolbox of MATLAB. (**b**) Distribution of angle, $\alpha$, between the cell orientation and maximum principal stress orientation. The distribution is composed of more than 8000 observations. Vertical size of (**a**) is 545 μm.

***Supplement 6. In the endothelial monolayer, the coarse actin structure tends to be aligned with the orientation of cell body.***

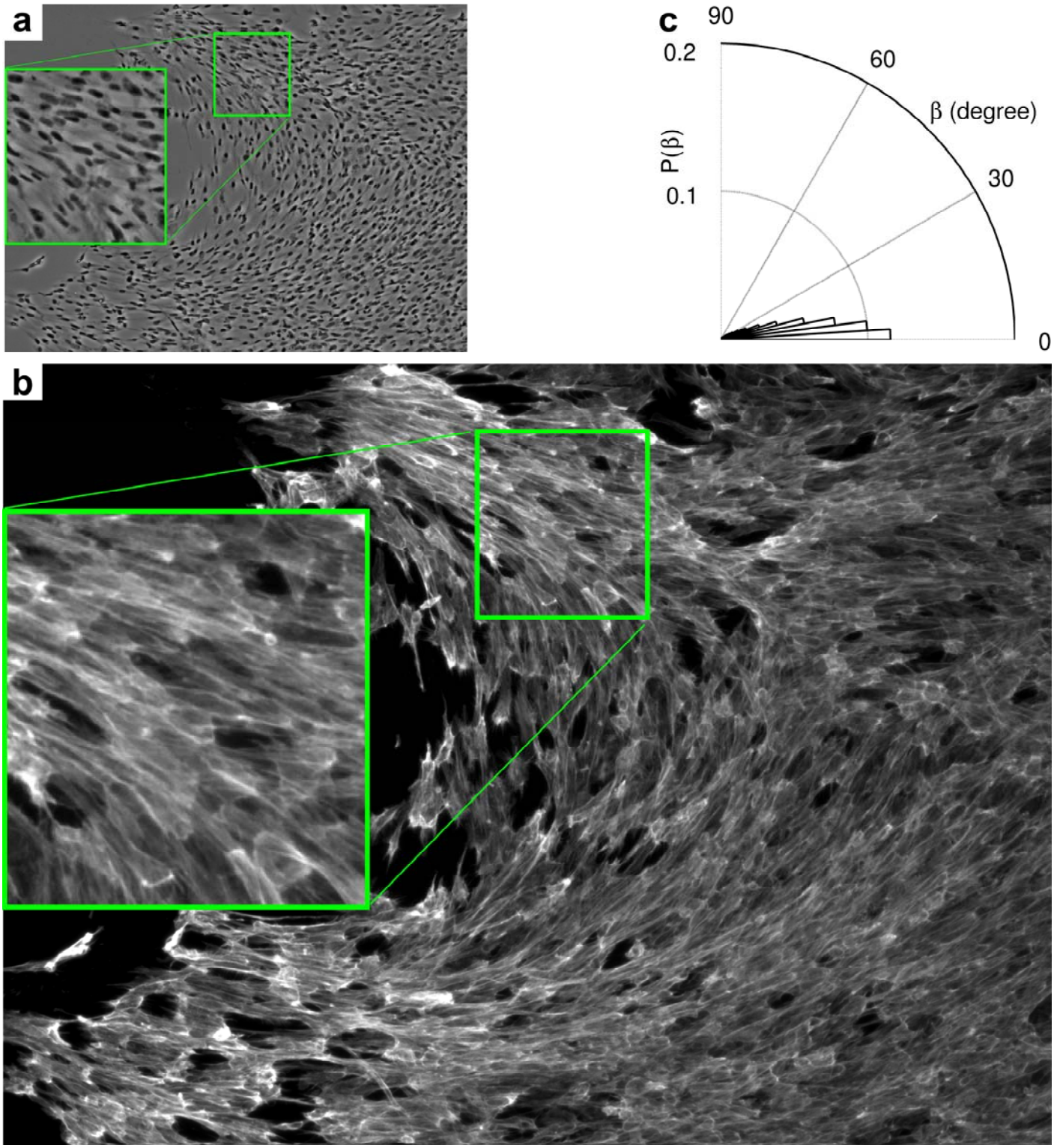


**Figure S6 | In RPME cell monolayers, the oriention of the cell body and the orientation of coarse actin structures tend to be aligned.** (**a**) Image of a RPME cell monolayer at 4X magnification. (**b**) Fluorescence image of actin structures (rhodamine phalloidin, Molecular Probes) [5]. (**c**) Distribution of angle, $\beta$, between the cell orientation from (**a**) and actin fiber orientation from (**b**). Local orientation of actin fibers is calculated using the same procedure used in calculating orientation of cells in (**a**) and in Fig. S5. Vertical size of (**a**) is 1700 μm.

***Supplement 7. Cells deep within the monolayer have cryptic lamellipodia.***

Using a wound/scratch assay, Farooqui and Fenteany [6] reported that cells located many rows behind the leading edge protrude underneath their neighbors. They called these protrusions "cryptic lamellidopia". To test whether submarginal cells within an expanding MDCK monolayer also extend cryptic lamellipodia we seeded an epithelial colony containing MDCK cells stably expressing either actin-GFP or α-actinin-RFP (Nelson Lab, Stanford). Using confocal microscopy during expansion of the colony we observed abundant cryptic lamellipodia at least 20 rows behind the leading edge (Fig. S7). Therefore wounding is not required for the existence of cryptic lamellipodia in submarginal cells.

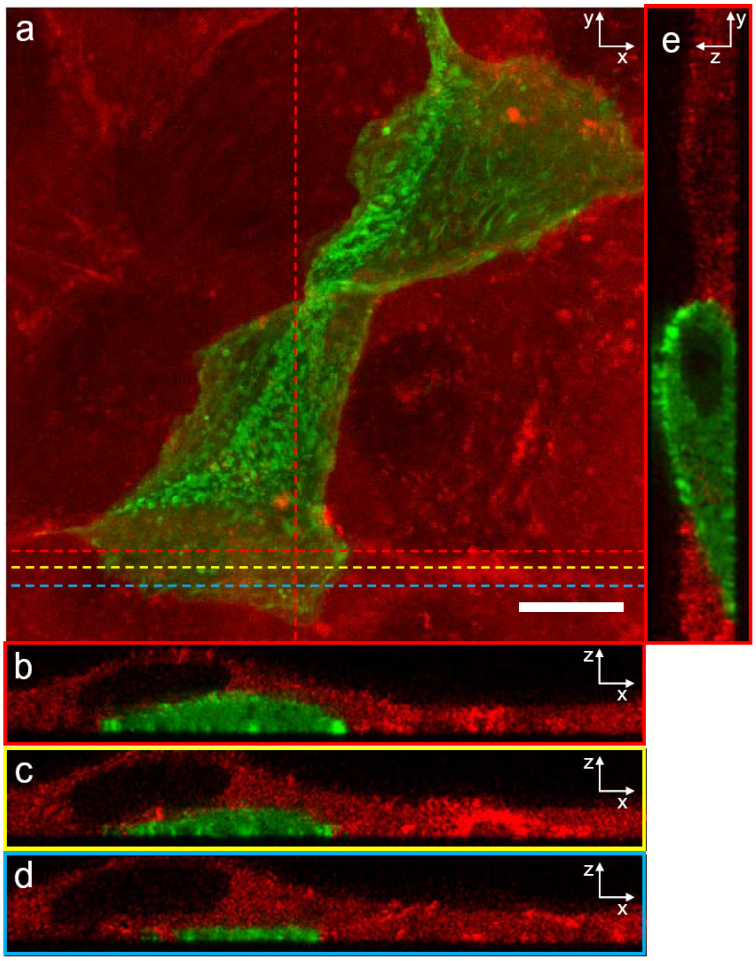


**Figure S7 | Observation of lamellipodial protrusion by the submarginal cells within an expanding MDCK cell monolayer.** (**a**) z-projection of submarginal cells (~20 cells away from the leading edge) in an expanding colony of MDCK cells expressing either actin-GFP or α-actinin-RFP. The bottom actin-GFP cell extends a cryptic lamellipodium under the neighboring α-actinin-RFP cell. The crytic lamellipodium is clearly visualized in panels (**b**), (**c**), and (**d**), which are xz sections (constant y) along the red, yellow, and blue dashed lines respectively. (**e**) yz section along the vertical red dashed line (constant x) shows the actin-GFP cell protruding under the α-actinin-RFP cell. Magnification 100X, resolution 1024×1024, scale bar 10 μm.

***Supplement 8. Local average normal stress does not account for local cell guidance.***

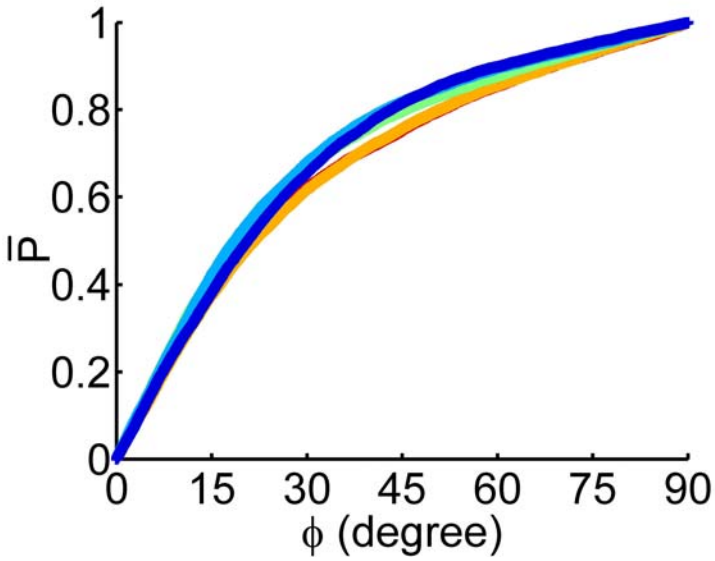


**Figure S8 | Cumulative probability distribution is independent of magnitude of local average normal stress.** For RPME cell monolayers, cumulative probability distribution of the alignment angle, $\phi$, is plotted as a function of quintiles of local average normal stress, curves from blue, to red are in the order of higher quintiles. Unlike the magnitude of local stress anisotropy shown in Fig. 2 i, the magnitude of local average normal stress is unrelated to the shape of $\overline{P}(\phi)$. Each curve has more than 8,000 observations.

***Supplement 9. Fluctuations, correlations, and the glass transition.***

When a force is applied to an elastic medium, its effects decay ideally as 1/r. But this decay is not to be confused with force fluctuations and the decay in their correlation function. To fix this latter idea, we consider the correlation decay in systems that might be considered as standards. We consider two examples that are not only instructive but also may bear parallels to the physics at play in the cellular monolayer.

We consider first the ideal and well-known case of the 2-D Ising model[39] of spin glasses above the glass transition temperature, Tc. In such systems the local spin interacts only with that of nearest neighbors. All interactions are strictly local. Even though all interactions are local the spin-spin correlation decays in space exponentially. [39] As the temperature decreases to approach Tc, moreover, successive local alignments of nearest neighbors causes long range order to emerge and the spin-spin correlation length to diverge.

We consider next an experimental model system for jamming in soft granular matter, namely, the 2-D assembly of soft, photoelastic disks. [40] When subjected to isotropic compression, force correlation length is as little as one disk diameter and the correlation function has close to a single exponential decay. But when subjected to mechanical shear, disk-disk contact forces line up into force chains, and as the jamming transition is approached the correlation length grows to span the full breadth of the system.

With these models in mind we now return to force correlation data in the monolayer (Fig. 5), which show evidence not only of force chains but also increase in the correlation length as cellular density increases. Taken together with previous observations of dramatic slowing of the cellular dynamics with increasing cellular crowding[41], one is led to the hypothesis that these monolayers operate physiologically in the neighborhood of a glass transition.

***Supplement 10. Mechanically guided motion as an integrative physiological principle.***

Although we have learned a great deal from recent studies of the standard model of the solitary cell crawling in isolation [7-11], in that system the physical constraints imposed by neighboring cells are not present and the innately cooperative mechanism at issue here is silenced. Consideration of the mechanical nature of the cell-cell interaction has led us to the observation that the orientation of local migration velocity aligns strongly with orientation of the maximal principal stress. This finding implies that each cell within the migrating epithelial or endothelial monolayer remodels itself locally so as to minimize shear stresses between itself and its immediate neighbors. This unanticipated finding complements other integrative physiological principles including Wolff's law of bone remodeling [12], Murray's law of vascular remodeling [13, 14], Kleiber's law of metabolic scaling[15-17], and McMahon's law of elastic similarity.[18, 19] In addition, this finding is closely related but complementary to Steinberg's hypothesis of differential adhesion for cell sorting and segregation.[20-38]

**Movie SM1 | Maps of cell-substrate and cell-cell stresses.** Time lapsed sequence of physical forces in the rat pulmonary microvascular endothelial (RPME) cell monolayer. As seen in the top left panel, the spindly cells move largely along long axis. During this motion, the cells apply on their substrate tractions that have dramatic spatio-temporal fluctuations (top right panel). The cells transfer the mechanically unbalanced part of the local traction to their neighbors, and on contrary to the tractions, the resulting average normal stresses have less frequent spatial fluctuations (bottom right panel). The intercellular stresses are highly anisotropic as the local maximum shear stresses are comparable to the average normal stress (bottom left panel). Cells in regions with higher stress anisotropy display stronger alignment between maximal principal stress and cell velocity. The sequence is 90 minutes long and 725x545 $\mu m^2$ in spatial extent.

**Movie SM2 | Collective migration occurs along local axis of highest normal stress.** Time lapsed sequence of rat pulmonary microvascular endothelial (RPME) cell monolayer overlapped with cell velocity vectors (red) and stress ellipses (blue). Long axis of the stress ellipse defines the local axis of highest normal stress, and the cell motion is locally aligned with this axis. The sequence is 90 minutes long and 725x545 $\mu m^2$ in spatial extent.

***Supplement References.***


1. **Ladoux, B. Cells guided on their journey. *Nature Physics* 5, 377-378 (2009).**
2. **Trepat, X. *et al.* Physical forces during collective cell migration. *Nature Physics* 5, 426-430 (2009).**
3. **An, S.S. *et al.* Hypoxia alters biophysical properties of endothelial cells via p38 MAPK- and Rho kinase-dependent pathways. *American Journal of Physiology - Cell Physiology* 289, C521-530 (2005).**
4. **Soule, H.D. *et al.* Isolation and Characterization of a Spontaneously Immortalized Human Breast Epithelial Cell Line, MCF-10. *Cancer Research* 50, 6075-6086 (1990).**
5. **J.-Victor Small, Klemens Rottner, Penelope Hahne & Anderson, K.I. Visualising the actin cytoskeleton. *Microscopy Research Technique* 47, 14 (1999).**
6. **Farooqui, R. & Fenteany, G. Multiple rows of cells behind an epithelial wound edge extend cryptic lamellipodia to collectively drive cell-sheet movement. *J Cell Sci* 118, 51-63 (2005).**
7. **Rubinstein, B., Fournier, M.F., Jacobson, K., Verkhovsky, A.B. & Mogilner, A. Actin-myosin viscoelastic flow in the keratocyte lamellipod. *Biophys J* 97, 1853-1863 (2009).**
8. **Mogilner, A. & Keren, K. The shape of motile cells. *Curr Biol* 19, R762-771 (2009).**

**9.** **Mogilner, A. Mathematics of cell motility: have we got its number? *J Math Biol* 58, 105-134 (2009).**
**10.** **Keren, K. *et al.* Mechanism of shape determination in motile cells. *Nature* 453, 475-480 (2008).**
**11.** **Lacayo, C.I. *et al.* Emergence of large-scale cell morphology and movement from local actin filament growth dynamics. *PLoS Biol* 5, e233 (2007).**
**12.** **Wolff, J. *The Law of Bone Remodeling*, Vol. (translation of the German 1892 edition). (Springer, 1986, Berlin Heidelberg New York; 1896).**
**13.** **Murray, C. The physiological principle of minimum work. I. The vascular system and the cost of blood volume. *Proceedings of the National Academy of Sciences USA* 12, 207-214 (1926).**
**14.** **Murray, C.D. The Physiological Principle of Minimum Work : A Reply. *J Gen Physiol* 14, 445 (1931).**
**15.** **Kleiber, M. Body size and metabolic rate. *Physiological Reviews* 27, 511–541. (1947).**
**16.** **White, C.R. Physiology: There is no single p. *Nature* 464, 691-693.**
**17.** **Kolokotrones, T., Van, S., Deeds, E.J. & Fontana, W. Curvature in metabolic scaling. *Nature* 464, 753-756.**
**18.** **McMahon, T. & Bonner, J. *On Size and Life*. (Scientific American Library, 1983).**
**19.** **McMahon, T.A. *Muscles, reflexes, and locomotion*. (Princeton University Press, Princeton, NJ; 1984).**
**20.** **Burdick, M.L. & Steinberg, M.S. Embryonic cell adhesiveness: do species differences exist among warm-blooded vertebrates? *Proc Natl Acad Sci U S A* 63, 1169-1173 (1969).**
**21.** **Gordon, R., Goel, N.S., Steinberg, M.S. & Wiseman, L.L. A rheological mechanism sufficient to explain the kinetics of cell sorting. *J Theor Biol* 37, 43-73 (1972).**
**22.** **Steinberg, M.S. On the Mechanism of Tissue Reconstruction by Dissociated Cells, Iii. Free Energy Relations and the Reorganization of Fused, Heteronomic Tissue Fragments. *Proc Natl Acad Sci U S A* 48, 1769-1776 (1962).**
**23.** **Steinberg, M.S. On the mechanism of tissue reconstruction by dissociated cells. I. Population kinetics, differential adhesiveness. and the absence of directed migration. *Proc Natl Acad Sci U S A* 48, 1577-1582 (1962).**
**24.** **Steinberg, M.S. Mechanism of tissue reconstruction by dissociated cells. II. Time-course of events. *Science* 137, 762-763 (1962).**
**25.** **Steinberg, M.S. Reconstruction of tissues by dissociated cells. Some morphogenetic tissue movements and the sorting out of embryonic cells may have a common explanation. *Science* 141, 401-408 (1963).**
**26.** **Steinberg, M.S. Cell movement in confluent monolayers: a re-evaluation of the causes of 'contact inhibition'. *Ciba Found Symp* 14, 333-355 (1973).**
**27.** **Steinberg, M.S. Adhesion-guided multicellular assembly: a commentary upon the postulates, real and imagined, of the differential adhesion hypothesis, with special attention to computer simulations of cell sorting. *J Theor Biol* 55, 431-443 (1975).**
**28.** **Steinberg, M.S. & Roth, S.A. Phases in Cell Aggregation and Tissue Reconstruction an Approach to the Kinetics of Cell Aggregation. *J Exp Zool* 157, 327-338 (1964).**
**29.** **Steinberg, M.S. & Wiseman, L.L. Do morphogenetic tissue rearrangements require active cell movements? The reversible inhibition of cell sorting and tissue spreading by cytochalasin B. *J Cell Biol* 55, 606-615 (1972).**
**30.** **Drawbridge, J. & Steinberg, M.S. Morphogenesis of the axolotl pronephric duct: a model system for the study of cell migration in vivo. *Int J Dev Biol* 40, 709-713 (1996).**
**31.** **Duguay, D., Foty, R.A. & Steinberg, M.S. Cadherin-mediated cell adhesion and tissue segregation: qualitative and quantitative determinants. *Dev Biol* 253, 309-323 (2003).**
**32.** **Foty, R.A., Pfleger, C.M., Forgacs, G. & Steinberg, M.S. Surface tensions of embryonic tissues predict their mutual envelopment behavior. *Development* 122, 1611-1620 (1996).**

**33.** **Foty, R.A. & Steinberg, M.S. Cadherin-mediated cell-cell adhesion and tissue segregation in relation to malignancy. *Int J Dev Biol* 48, 397-409 (2004).**
**34.** **Foty, R.A. & Steinberg, M.S. The differential adhesion hypothesis: a direct evaluation. *Dev Biol* 278, 255-263 (2005).**
**35.** **Poole, T.J. & Steinberg, M.S. Different modes of pronephric duct origin among vertebrates. *Scan Electron Microsc*, 475-482 (1984).**
**36.** **Steinberg, M.S. Adhesion in development: an historical overview. *Dev Biol* 180, 377-388 (1996).**
**37.** **Wiseman, L.L., Steinberg, M.S. & Phillips, H.M. Experimental modulation of intercellular cohesiveness: reversal of tissue assembly patterns. *Dev Biol* 28, 498-517 (1972).**
**38.** **Beysens, D.A., Forgacs, G. & Glazier, J.A. Cell sorting is analogous to phase ordering in fluids. *Proc Natl Acad Sci U S A* 97, 9467-9471 (2000).**
**39.** **McCoy, B. & Wu, T.T. *The Two-Dimensional Ising Model*, Edn. 1. (Harvard University Press, 1973).**
**40.** **Majmudar, T.S. & Behringer, R.P. Contact force measurements and stress-induced anisotropy in granular materials. *Nature* 435, 1079-1082 (2005).**
**41.** **Angelini, T.E. *et al.* Glass-like dynamics of collective cell migration. *Proc Natl Acad Sci U S A* (Early edition: http://www.pnas.org/content/early/2011/02/09/1010059108.full.pdf).**